Journal of Constructional Steel Research 122 (2016) 80–93

Contents lists available at ScienceDirect

Journal of Constructional Steel Research

Optimum design of cold-formed steel beams using Particle Swarm Optimisation method

Jun Ye *, Iman Hajirasouliha, Jurgen Becque, Abolfazl Eslami

Department of Civil Engineering and Structural Engineering, The University of Sheffield, Sheffield, UK

ARTICLE INFO

Article history:
Received 14 October 2015
Received in revised form 10 February 2016
Accepted 13 February 2016
Available online xxxx

Keywords:
Cold-formed steel
Optimisation
Flexural strength
Effective width method
Direct strength method
Finite Element Analysis

ABSTRACT

Applying optimisation techniques to the design of cold-formed steel (CFS) sections can lead to more economical and efficient design solutions. However, a crucial factor in such an optimisation is to arrive at a solution which is practical and fits within the constraints of the fabrication and construction industries. Targeting this objective, a comprehensive investigation was conducted on the practical optimisation of CFS beams using a Particle Swarm Optimisation (PSO) method. Six different CFS channel section prototypes were selected and then optimised with respect to their flexural strength, determined according to the effective width based provisions of Eurocode 3 (EC3) part 1–3. Comparing the capacities of the optimised sections to those of the original channel sections with the same amount of structural material, significant improvements were obtained. The accuracy of the optimisation procedure was assessed using experimentally validated nonlinear Finite Element (FE) analyses accounting for the effect of imperfections. The results indicated that, using the same amount of material, the optimum sections offered up to 25% and 75% more flexural strength for laterally braced and unbraced CFS beams, respectively, while they also satisfied predefined manufacturing and design constraints. Therefore, the proposed optimisation methodology has the potential to prove useful in practical design applications.

1. Introduction

Cold-formed steel (CFS) structural elements and systems are widely used in the construction industry, for instance in trusses, modular building panels, stud walls, purlins, side rails, cladding and even as the primary load-bearing structure in low- to mid-rise buildings. Compared to their hot-rolled counterparts, CFS members are often found to be more economical and efficient, due to inherent advantages such as light weight, ease and speed of erection and a greater flexibility in manufacturing cross-sectional profiles and sizes. Many cold-rolling companies have the ability to custom roll sections on demand, adapted to certain particular applications. It is this versatility on the manufacturing side which makes the problem of finding optimal cross-sectional shapes of great interest to structural engineers. In general, cross-sectional optimisation methods of CFS members can be classified into two categories. One can either aim to determine an optimal cross-sectional shape without any initial restrictions on its form (shape optimisation), or optimise the relative dimensions of a cross-section with a predefined shape (size optimisation).

As an example of shape optimisation, Liu et al. [1] introduced a knowledge-based approach for optimisation of CFS column sections. Initial knowledge about what constitutes a 'good' design is thereby established by training a Bayesian classification tree learning algorithm. This knowledge is subsequently used to reduce the global design space to a lower dimensional expert-based feature space. The results showed that optimised cross-sectional shapes can demonstrate a much higher capacity (by up to 300%) compared to conventional cross-sections. Moharrami et al. [2] found the optimal shapes of open CFS cross-sections in compression, using a fixed coil width and plate thickness. The compressive strength of a given section was thereby evaluated using a combination of the Finite Strip Method (FSM) and the Direct Strength Method (DSM). However, their study did not consider manufacturing and construction constraints and, therefore, highly complex shapes were identified that are not suitable for practical applications due to their high manufacturing costs and the difficulty in connecting to other elements. The resulting shapes also did not classify as pre-qualified sections under the DSM rules, thus questioning the optimisation approach. Leng et al. [3] later improved this method by incorporating end-user constraints and limiting the numbers of rollers in the manufacturing process. CFS columns with different lengths were optimised and more practical shapes were obtained, which however still did not meet the DSM pre-qualification conditions.

Several research projects have previously been carried out aimed at optimising the relative dimensions of predefined conventional CFS cross-sections such as *C*–, *Z*–, or ∑– shapes. Adeli and Karim [4] developed a Neural Network methodology for the optimum cross-sectional design of CFS beams, considering conventional hat, *I*–, and *Z*– cross-sections. Using Micro Genetic Algorithms, Lee et al. [5,6] optimised the

* Corresponding author.
E-mail address: jye2@sheffield.ac.uk (J. Ye).

http://dx.doi.org/10.1016/j.jcsr.2016.02.014

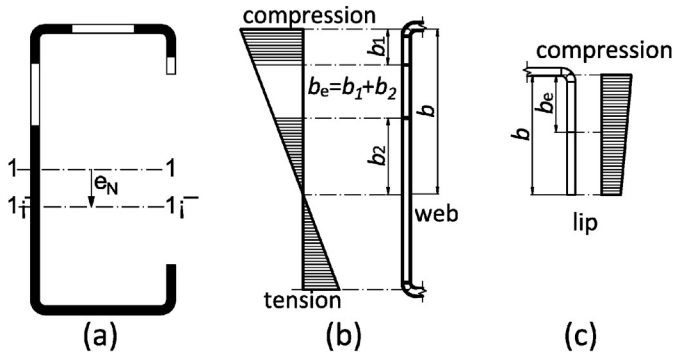

Fig. 1. Effective width of (a) lipped channel; (b) internal compression element; and (c) outstand compression element.

geometry of CFS channel beams and columns under a uniformly distributed load and a compressive axial load, respectively. Their numerical results were presented in the form of optimum design curves for various load levels. Tran and Li [7] presented a theoretical study on the optimisation of lipped channel beams subjected to uniformly distributed transverse loading. The failure modes of local, distortional and global buckling, as well as yielding, in combination with deflection limits, were considered and the optimisation process aimed to minimize the coil width. The shape optimisation of CFS channel beams with 'drop' flanges (rounded return lips shaped like a water drop) was described by Magnucki et al. [8]. They found that channel beams with closed drop flanges can offer better performance compared to beams with open drop flanges or standard lips. More recently, Ma et al. [9] optimised CFS compression and bending members according to EC3 [10] by using the genetic algorithm toolbox in Matlab [11]. They investigated the influence of the column length and the shift of the effective centroid, induced by local/distortional buckling, on the optimum design solutions. The practicality of their solutions was guaranteed by constraining the overall shape of the cross-section to a channel, but no additional manufacturing or construction constraints were taken into account in the study.

The research presented in this paper aimed to develop a new practical framework to optimise CFS channel beam sections while considering both manufacturing and design constraints. The Particle Swarm Optimisation (PSO) method was thereby adopted to achieve optimum design solutions according to the European design guidelines for CFS structural members [10–12]. The complexity of the non-linear optimisation problem was managed by using the Eurocode design regulations as a 'black-box' tool in the optimisation procedure. The adequacy of Eurocode 3 in predicting increasing/decreasing trends in capacity as a result of changing geometric parameters and adding features like stiffeners and return lips was then evaluated by modelling the optimal sections using detailed FE models accounting for material and geometric non-linearity, as well as imperfections. The developed FE models were first validated against existing experimental results.

2. Design of CFS members based on EC3

In this study, the flexural strength of CFS sections was calculated based on the Effective Width Method, following the provisions of EN1993-1-3 [10] and EN1993-1-5 [11]. The adopted design procedure is described briefly in the following sections.

2.1. Design for local buckling

In Eurocode 3, the effect of local buckling is considered through the effective width concept. It is based on the observation that local buckling causes a loss of compressive stiffness in the centre of a plate supported along both longitudinal edges (labelled an 'internal' plate element in EC3), or along the free edge of a plate supported along one longitudinal edge (an 'outstand' element) as a result of non-linear effects. The corner zones of the cross-section consequently become the main load-bearing areas and are idealized in the effective width concept as carrying the totality of the load. The effective area of a sample cross-section is indicated in solid black line in Fig. 1. It is thereby noted that local buckling causes the centroid of the effective cross-section to shift over a distance e_N relative to the original centroid of the gross cross-section. According to EN1993-1-5 [11], the effective widths of internal and outstand compression elements are given by (see Fig. 1):

$$\rho = \frac{b_e}{b} = \begin{cases} \frac{1}{\lambda_l}\left(1-\frac{0.055(3+\psi)}{\lambda_l}\right) & \text{for internal compression element} \\ \frac{1}{\lambda_l}\left(1-\frac{0.188}{\lambda_l}\right) & \text{for outstand compression element} \end{cases} \quad (1)$$

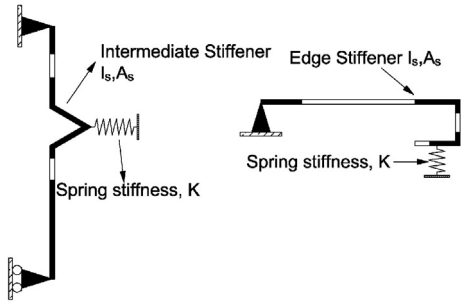

Fig. 2. Simplified models for distortional buckling calculations.

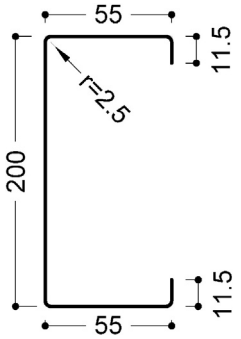

Fig. 3. Standard CFS beam cross-section (TATA-A3709).

with

$$\lambda_l = \sqrt{\frac{f_y}{\sigma_{cr}}}. \tag{2}$$

In Eq. (1) ρ is the reduction factor on the plate width and b and b_e are the total and the effective width of the plate, respectively. The slenderness ratio λ_l relates the material yield stress f_y to the elastic local buckling stress of the plate σ_{cr} and ψ is the ratio of the end stresses in the plate. It is worth mentioning that, in principle, Eurocode 3 calculates the effective cross-section A_{eff} using the yield stress f_y in Eq. (2), while some design standards (in particular the North-American [13] and Australian/New Zealand [14] specifications) use the global buckling stress of the beam. It should also be noted that the calculation of the effective cross-section in bending is an iterative process, since the neutral axis of the effective cross-section shifts over a distance which depends on the loss of effective section in the flange and the upper portion of the web and this, in turn, affects the stress distribution. Although not required by EC3 guidelines, full iterations to convergence were carried out in this study.

2.2. Design for distortional buckling

Distortional buckling of a CFS section is a process which requires in-plane as well as out-of-plane displacements of some of the constituent plates. Specifically related to lipped channels, it can be seen as lateral-torsional buckling of the flange-lip subassembly, but distortional buckling can also occur in the web when intermediate stiffeners are included.

While EC3 accounts for local buckling through a reduction of the effective width of the constituent plates, distortional buckling is instead taken into account by reducing the effective plate thickness. The elastic distortional buckling stress, required for the calculation of the distortional slenderness $\lambda_d = \sqrt{f_y/\sigma_{cr,s}}$, is obtained through a simplified model where the restraining effect of the adjacent plates is simulated by elastic springs, as illustrated in Fig. 2. The elastic buckling stress of the plate-stiffener assembly $\sigma_{cr,s}$ is then given by:

$$\sigma_{cr,s} = \frac{2\sqrt{KEI_s}}{A_s} \tag{3}$$

where E is the modulus of elasticity, I_s is the second moment of area of the stiffener about an axis through its centroid parallel to the plate, K is the spring stiffness per unit length and A_s is the stiffener area. The spring stiffness K is determined by applying a unit load $f = 1$ (per unit length) to the full cross-section at the centroid of the stiffener assembly and by calculating the corresponding displacement.

EC3 provides the option to refine the local slenderness ratio λ_l of the plates using an iterative process based on the following equation:

$$\lambda_{l,red} = \lambda_l \sqrt{\chi_d} \tag{4}$$

where χ_d is a prescribed function of the distortional buckling slenderness λ_d. When calculating λ_d in each iteration, f_y should be replaced by $\sigma_{com} = \chi_d \cdot f_y$. This option provided by EC3 was implemented in the study and the iterations continued until $\chi_{d,n} \approx \chi_{d,(n-1)}$.

Table 1
Selected prototypes, design variables and constraints.

Prototype	Prototype section	Design variables	Constraints based on EC3	Comments	Manufacturing & practical limitations (mm)
①	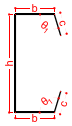	$x_1 = c/b$ $x_2 = b/l$ $x_3 = \theta_1$	$0.2 \le c/b \le 0.6$ $b/t \le 60$ $c/t \le 50$ $h/t \le 500$ $\pi/4 \le \theta_1 \le 3/4\pi$	EN1993-1-3 Table 5.1 and Equation (5.2a), Clause 5.5.3.2(1)	$h \ge 100$ $b \ge 30$ $c \ge 10$
②	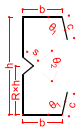	$x_1 = c/b$ $x_2 = b/l$ $x_3 = R$ $x_4 = \theta_1$ $x_5 = \theta_2$ $x_6 = s$	$0.2 \le c/b \le 0.6$ $b/t \le 60$ $c/t \le 50$ $h/t \le 500$ $\pi/4 \le \theta_1 \le 3/4\pi$ $\pi/6 \le \theta_2 \le \pi/2$	EN1993-1-3 Table 5.1 and Equation (5.2a), Clause 5.5.3.2(1)	$h \ge 100$ $b \ge 30$ $c \ge 10$ $0.1 \le R \le 0.9$
③	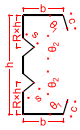	$x_1 = c/b$ $x_2 = b/l$ $x_3 = R$ $x_4 = \theta_1$ $x_5 = \theta_2$ $x_6 = s$	$0.2 \le c/b \le 0.6$ $b/t \le 60$ $c/t \le 50$ $h/t \le 500$ $\pi/4 \le \theta_1 \le 3/4\pi$ $\pi/6 \le \theta_2 \le \pi/2$	EN1993-1-3 Table 5.1 and Equation (5.2a), Clause 5.5.3.2(1)	$h \ge 100$ $b \ge 30$ $c \ge 10$ $0.1 \le R \le 0.4$
④		$x_1 = c/b$ $x_2 = d/b$ $x_3 = b/l$ $x_4 = \theta_1$	$0.2 \le c/b \le 0.6$ $0.1 \le d/b \le 0.3$ $b/t \le 90$ $c/t \le 60$ $d/t \le 50$ $h/t \le 500$ $\pi/4 \le \theta_1 \le 3/4\pi$	EN1993-1-3 Table 5.1 and Equation (5.2a,b), Clause 5.5.3.2(1)	$h \ge 100$ $b \ge 30$ $c \ge 10$ $d \ge 5$
⑤	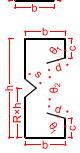	$x_1 = c/b$ $x_2 = d/b$ $x_3 = b/l$ $x_4 = R$ $x_5 = \theta_1$ $x_6 = \theta_2$ $x_7 = s$	$0.2 \le c/b \le 0.6$ $0.1 \le d/b \le 0.3$ $b/t \le 90$ $c/t \le 60$ $d/t \le 50$ $h/t \le 500$ $\pi/4 \le \theta_1 \le 3/4\pi$ $\pi/6 \le \theta_2 \le \pi/2$	EN1993-1-3 Table 5.1 and Equation (5.2a,b), Clause 5.5.3.2(1)	$h \ge 100$ $b \ge 30$ $c \ge 10$ $d \ge 5$ $0.1 \le R \le 0.9$
⑥	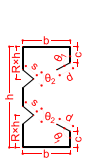	$x_1 = c/b$ $x_2 = d/b$ $x_3 = b/l$ $x_4 = R$ $x_5 = \theta_1$ $x_6 = \theta_2$ $x_7 = s$	$0.2 \le c/b \le 0.6$ $0.1 \le d/b \le 0.3$ $b/t \le 90$ $c/t \le 60$ $d/t \le 50$ $h/t \le 500$ $\pi/4 \le \theta_1 \le 3/4\pi$ $\pi/6 \le \theta_2 \le \pi/2$	EN1993-1-3 Table 5.1 and Equation (5.2a,b), Clause 5.5.3.2(1)	$h \ge 100$ $b \ge 30$ $c \ge 10$ $d \ge 5$ $0.1 \le R \le 0.4$

Table 2
Dimensions of optimal solutions for laterally restrained beams.

Prototype	h (mm)	b (mm)	c (mm)	d (mm)	θ_1 (°)	θ_2 (°)	s (mm)	R
①	227	32	20	–	90	–	–	–
②	214	33	20	–	90	45	10	0.85
③	215	33	20	–	90	90	10	0.1
④	215	37	17	5	90	–	–	–
⑤	204	37	12	5	135	67	10	0.9
⑥	193	39	17	6	135	90	10	0.1

2.3. Design for global buckling

According to EC3, the design of CFS members for global buckling requires the calculation of a global slenderness. For CFS beam elements, the slenderness for lateral-torsional buckling is defined as

$$\lambda_{LT} = \sqrt{\frac{W_{eff} f_y}{M_{cr}}} \tag{5}$$

where M_{cr} is the elastic lateral-torsional buckling moment based on the gross cross-section, and W_{eff} is the effective section modulus.

3. Definition of optimisation problem

The optimisation procedure aimed to optimise CFS cross-sections with regard to their bending capacity, determined according to EC3. The starting point of the optimisation was the commercially available channel section shown in Fig. 3. The thickness of $t = 1.2$ mm and the total coil width of $l = 333$ mm were kept constant in the optimisation process, so that the total material use was also kept identical for all cross-sections. The radius of the rounded corners (measured along the heart line of the section), the elastic modulus and the Poisson's ratio were taken as 2.5 mm, 210 GPa and 0.3, respectively. The yield strength of the steel was assumed to be $f_y = 350$MPa.

To ensure that the optimisation process resulted in practically useful cross-sections, the following measures were taken:

1. The basic overall shape of the cross-section was restricted to a channel. In current construction practice, channels (and Z-sections) are the most commonly used CFS beam sections. The succession of flat plate elements within the cross-section permits a straightforward manufacturing process and allows for easy connections with trapezoidal steel deck or other roof/floor systems, as well as bridging, cleat plates, etc. This stands in contrast with the often complex and curved shapes typically encountered as the result of unrestricted shape optimisation procedures. This objective was achieved by considering six different prototypes, listed in Table 1. All prototypes are based on a channel shape, but they allow the inclusion of a single web stiffener, double web stiffeners, inclined lips and double-fold (return) lips. These additions are typically within the capability of commercial cold-rolling enterprises. Each prototype was optimised individually, after which the overall optimum among the six optimised prototypes was identified.
2. In practical situations, additional constraints typically come into play. These constraints may be quite case-dependent and may, for instance, be related to the ability to connect the beam to other elements, or be imposed by the manufacturing process itself. In this particular case the following constraints were imposed:
   a. The width of the flanges was required to be at least 30 mm in order to connect trapezoidal decking or plywood boards to the beam by means of screws. This width was determined after consultation with the industrial partner on the project.
   b. The lip needs to be of a sufficient length. A lip of, for instance, 1 mm or 2 mm length cannot be rolled or brake-pressed. The industrial partner on the project suggested a minimum length of 5–10 mm. Therefore, as indicated in Table 1, $c \geq 10$ mm was imposed for a single lip and combined with $d \geq 5$ mm for a return lip.
   c. The height of the web was specified to be at least 100 mm in order to allow a connection to be made (e.g. to a cleat plate) with at least two bolts and/or for bridging to be connected.

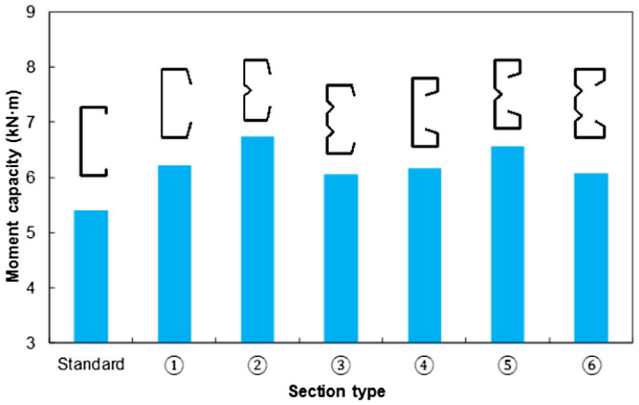

Fig. 5. Comparison of the flexural strength of standard and optimised cross-sections for laterally braced beams.

One of the major advantages of the PSO algorithm is that these constraints can easily be altered and others added. The constraints merely result in a restriction of the search space of the particle swarm.

In addition to the practical constraints mentioned above, the EC3 design rules also impose certain limits on the plate width-to-thickness ratios, the relative dimensions of the cross-section and the angle of the edge stiffeners. These constraints were also taken into account in

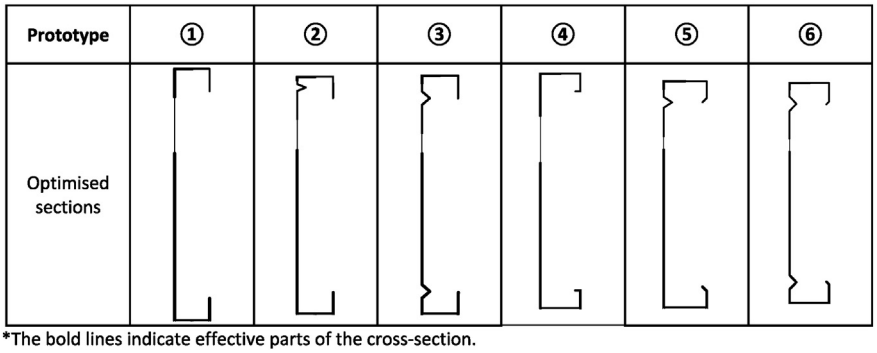

Fig. 4. Optimal cross-sections for laterally restrained beams using different prototypes.

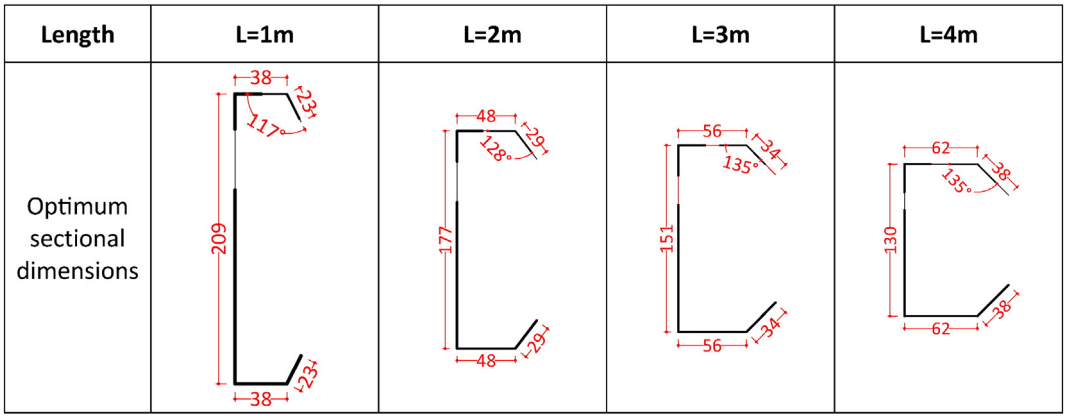

Fig. 6. Optimised results for member capacity of lipped channel beams.

the optimisation procedure and are listed in Table 1 under the heading 'Constraints based on EC3'.

Finally, the opening angle θ_2 and the length s of the intermediate stiffeners was limited within the ranges of $\pi/6$ to $\pi/4$ and 5 mm to 10 mm, respectively. The optimisation was conducted separately for laterally braced and un-braced beams, as discussed in the following sections.

It is clear that both the choice of the prototypes and the addition of practical constraints significantly restrict the solution space. An unconstrained 'free-form' optimisation would most likely result in a cross-section with a higher ultimate capacity, with this 'overall optimum' solution not being contained within the current restricted search space. However, the aim of the research was to produce cross-sections with practical relevance and the prototypes in Table 1 were decided on after consultation with the industry partner.

It is also noted that, while the chosen constraints are quite specific, the proposed optimisation framework is generally applicable and can be used in combination with different prototypes and different constraints.

4. Particle Swarm Optimisation

The objective of the optimisation was to maximize the bending capacity of CFS beams according to EC3, subject to the design constraints and practical limitations listed in Table 1. Due to the high nonlinearity of the problem, a Particle Swarm Optimisation (PSO) method was adopted. PSO is a population-based algorithm, which is inspired by the swarming behaviour of biological populations such as flocks of birds or schools of fish. The mechanism has some parallels with evolutionary computational techniques, such as Genetic Algorithms (GA). An initial population of solutions is randomly selected, but unlike GA, solutions are optimised by updating generations without any evolution operators such as crossover or mutation. The potential solutions in PSO, called particles, move in the problem space by following the current optimum particles. This usually leads to a better efficiency in terms of computational cost and, therefore, a faster convergence rate compared to GA [15,16].

A swarm is comprised of N particles moving around a D-dimensional search space, in which each particle represents a potential solution to the optimisation problem. The position and velocity vectors of ith particle are $\rho_i = \{\rho_{i1}, \rho_{i2}, \ldots, \rho_{ij}, \ldots, \rho_{iD}\}$ and $V_i = \{v_{i1}, v_{i2}, \ldots, v_{ij}, \ldots, v_{iD}\}$, respectively, where $i = 1, 2, 3, \ldots N$. The particles then fly through the space in search for the global optimal solution. In each iteration step, the ith particle updates its position and velocity based on a combination of: a. its personal best position over its history, and b. the position of the particle within the swarm with the best position in the previous iteration. This can mathematically be expressed as:

$$V_i^{k+1} = w \cdot V_i^k + c_1 \cdot r_1 \cdot \left(P_{best,\ i}^k - \rho_i^k\right)/\Delta t + c_2 \cdot r_2 \cdot \left(G_{best}^k - \rho_i^k\right)/\Delta t \quad (6)$$

$$\rho_i^{k+1} = \rho_i^k + V_i^{k+1} \cdot \Delta t \quad (7)$$

where the subscripts i and k denote the particle and the iteration number, respectively. Δt is the time increment. The vectors $P_{best,i}^k = \{p_{i1}, p_{i2}, \ldots, p_{ij}, \ldots, p_{iD}\}$ and $G_{best}^k = \{g_1, g_2, \ldots, g_D\}$ denote the best position of the ith particle over its history up to iteration k, and the position of

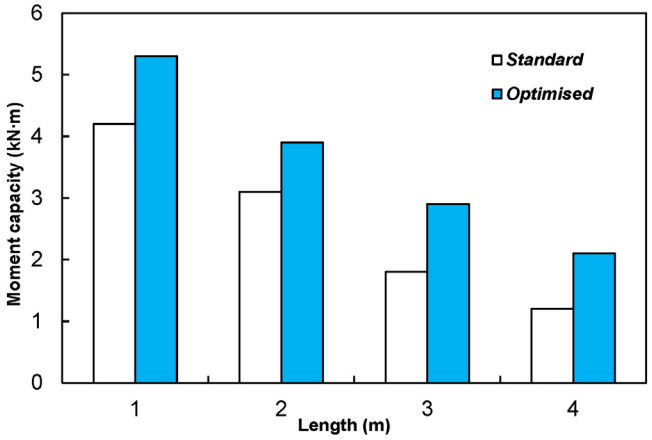

Fig. 7. Comparison of the flexural strength of the optimised and standard cross-sections for laterally unbraced beams.

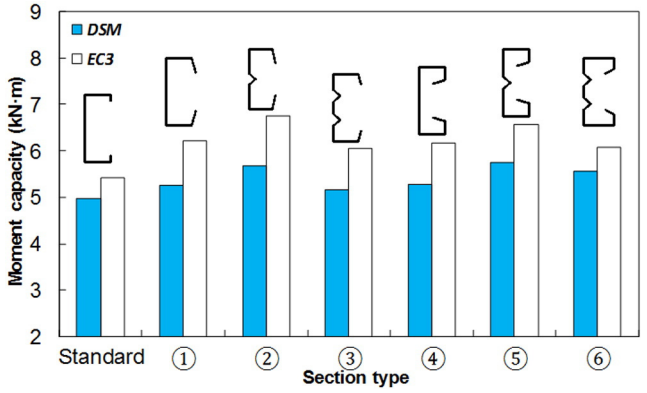

Fig. 8. Comparison of the flexural strength of the optimised and standard cross-sections for laterally braced beams obtained using the DSM and EC3.

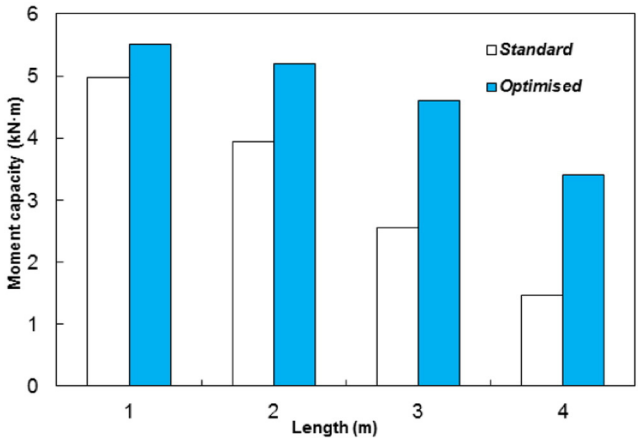

Fig. 9. Comparison of the flexural strength of the optimised and standard cross-sections for laterally unbraced beams obtained using the DSM.

the best particle in the swarm in iteration k, respectively. Also, c_1 is a cognitive parameter indicating the degree of confidence in the solution obtained from each individual particle, whereas c_2 is a social parameter to reflect the confidence level that the swarm as a whole has reached a favourable position. In addition, r_1 and r_2 are two independent random numbers uniformly distributed between 0 and 1, and w is the inertial weight used to preserve part of the previous velocity of the particles during the optimisation process. Perez [17] suggested the following conditions to improve the convergence of a PSO problem:

$$0 < c_1 + c_2 < 4 \tag{8}$$

$$\frac{c_1 + c_2}{2} - 1 < w < 1 \tag{9}$$

Using a large value of the inertial weight factor w facilitates global searching, which is particularly crucial in the initial stages of the optimisation. On the contrary, a small value of w tends to localise the search pattern, a technique which can be used to accelerate the convergence in the later stages. In the problem under study a dynamic variation of the inertial weight was used to improve the global/local search behaviour by linearly decreasing w with successive iterations as follows [18]:

$$w_{k+1} = w_{\max} - \frac{w_{\max} - w_{\min}}{k_{\max}} k \tag{10}$$

where k and $k_{\max}$ are the iteration and total iteration number, respectively, and $w_{\max}$ and $w_{\min}$ are the maximum and the minimum values of the inertial weight factor.

5. Optimisation of CFS beams

In practical applications, the boundary conditions of laterally braced and laterally unbraced beams represent two distinct situations. The laterally braced beams are representative, for instance, of floor beams connected to a steel deck with concrete topping, where the compression flange is continuously supported. On the other hand, roof purlins subject to wind uplift where the rotational stiffness of the roof diaphragm is insufficient to provide full restraint should be designed as laterally unbraced beams with a representative effective length, and the effects of lateral-torsional buckling should be taken into account. Therefore, in this study, laterally braced and unbraced beams are optimised independently.

Table 3
Local and distortional ultimate strengths for laterally braced beams obtained using the DSM.

Section	Local buckling (kN·m)	Distortional buckling (kN·m)
Standard	5.52	4.98
①	5.25	5.47
②	7.34	5.68
③	5.71	5.16
④	5.27	5.27
⑤	5.94	5.74
⑥	6.07	5.56

Table 4
Local, distortional, and global ultimate strengths for laterally unbraced beams obtained using the DSM.

Length (m)	Section	Local Buckling Strength (kN·m)	Distortional Buckling Strength (kN·m)	Global buckling strength (kN·m)
1	Standard	5.53	4.98	6.59
	Optimised	5.48	5.66	5.5
2	Standard	5.53	4.98	3.94
	Optimised	5.54	5.28	5.2
3	Standard	5.53	4.98	2.56
	Optimised	4.98	4.61	4.6
4	Standard	5.53	4.98	1.47
	Optimised	4.22	4.15	3.4

5.1. Laterally braced beams

In many practical applications the CFS beams are laterally restrained, for instance by the presence of a floor system. In that case the optimisation problem can be formulated as a maximization problem, defined by:

$$\max f(x) = W_{eff} f_y / \gamma_{M0} \qquad u_{\min} \le x_i \le u_{\max} \quad \text{for } i = 1, \ldots, N \tag{11}$$

where $f(x)$ is the design moment resistance of a cross-section about the major axis and W_{eff} is the effective section modulus, as introduced in Section 2. Also, γ_{M0} is the partial safety factor prescribed by EC3 for the ultimate limit state, which is equal to 1.0. For each design variable x_i, the lower and upper bounds $\mu_{\min}$ and $\mu_{\max}$ are determined by the EC3 design constraints as well as the manufacturing limitations summarised in Table 1.

The selected prototypes in this study were aimed at investigating the effects of changing the relative geometric dimensions of the cross-section and the configurations of the edge and intermediate stiffeners (see Table 1). The optimisation framework required the development of two distinct pieces of software, developed in Matlab [19]: a programme implementing the EC3 design rules and further used as a 'black box', and a programme carrying out the PSO. The population of the particle swarm was taken as 100 for all prototype sections. To obtain good convergence, the number of iterations was set to 100 for prototypes ① to ④, while this was increased to 160 for prototypes ⑤ and ⑥ to accommodate the larger number of design parameters. The maximum and minimum inertial weight factors were chosen as 0.95 and 0.4, respectively. Each of the prototypes was optimised three times to ensure consistent results were obtained. The maximum

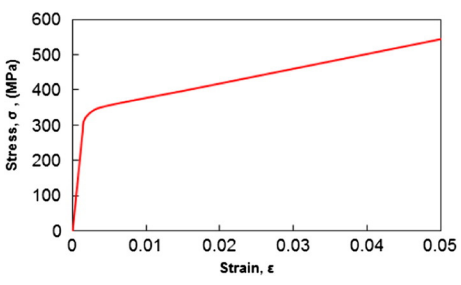

Fig. 10. Stress–strain behaviour of CFS plate used in the FE modelling.

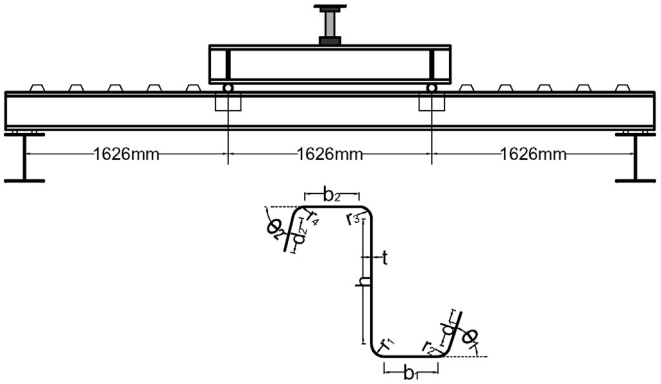

Fig. 11. Schematic illustration of Yu and Schafer's [31,32] distortional buckling test set-up and cross-sectional geometry.

difference in ultimate capacity encountered between the three runs was less than 10%. Out of the three resulting cross-sections, the one with the highest capacity was selected.

Table 2 shows the dimensions of the optimised sections for prototypes ① to ⑥. The effective cross sections of the optimum solutions are also illustrated in Fig. 4. The flexural strengths of the optimised cross-sections, as well as the standard cross-section taken as a starting point, are compared in Fig. 5. The results indicate that the optimised shapes offer a significantly higher moment capacity (up to 25% higher) compared to the original section.

The results in Fig. 5 also indicate that the most efficient prototype is a lipped channel section with one stiffener placed in the web. While adding one stiffener increased the capacity of the optimised section by 25%, adding two stiffeners in a symmetric arrangement (prototype ③) actually reduced the flexural capacity of the channel by 12.4% compared to prototype ①. This is due to the fact that, when the total developed length of the cross-section is kept constant, the height of the cross-section is reduced by adding the additional web stiffener, while, in a symmetric arrangement, the stiffener is ineffective in the tension zone. It is also noted that none of the imposed practical constraints, listed in the rightmost column of Table 1 turned out to be critical.

It should also be mentioned that the authors have recently developed a new type of 'folded-flange' section, which can offer even higher bending moment capacities compared to the more conventional channel sections discussed above. However, the effective width method in EC3 cannot directly be used to design this folded-flange section. Therefore, a separate study has been dedicated to it [20].

5.2. Laterally unbraced beams

Laterally unbraced beams with low lateral and/or torsional stiffness may buckle in combined bending about the minor axis and twisting. For a simply supported channel beam subjected to equal but opposite end moments about the major axis, the critical lateral-torsional buckling load M_{cr} can be calculated in terms of the span length and the section properties of the gross section as follows:

$$M_{cr} = \frac{\pi}{L}\sqrt{EI_y\left(GJ + \frac{\pi^2 EI_w}{L^2}\right)} \tag{12}$$

where EI_y is the flexural rigidity about the minor axis, EI_w is the warping rigidity, GJ is the torsional rigidity and L indicates the span length. The EC3 reduction factor χ_{LT}, accounting for lateral-distortional buckling, can then be obtained using the slenderness λ_{LT}

Table 5
Cross-sectional dimensions.

Specimen	h (mm)	b_2 (mm)	d_2 (mm)	Θ_2 (deg)	b_1 (mm)	d_1 (mm)	Θ_1 (deg)	r_3 (mm)	r_4 (mm)	r_2 (mm)	r_1 (mm)	t (mm)	f_y (MPa)
D8.5Z120-4	196	53.4	19.4	54.2	49.8	20.8	50.2	7.5	7.5	7.5	7.5	3	423
D8.5Z115-1	197	56.9	17	48.3	48.5	17.5	48.3	7.5	7.5	8.5	8.5	2.96	453
D8.5Z092-3	198	55.6	20.6	51.9	49.1	20.1	51.6	5.9	5.9	6.9	6.9	2.27	397
D8.5Z082-4	200	53.8	20.8	48.5	49.2	21.2	51.3	6	6	7	7	2.06	408
D8.5Z065-7	199	51.3	17.3	50	49.9	16.9	49.3	7.2	7.2	8.2	8.2	1.63	430
D8.5Z065-4	198	49.5	17.5	47.3	46.6	12.6	51.2	7.2	7.2	6.2	6.2	1.57	401
D11.5Z092-3	270	75.3	19.3	49.3	76.3	18.3	49.5	6.9	6.9	6.9	6.9	2.26	483
D11.5Z082-4	274	75.4	18.4	48.4	74.3	18.3	49.9	7	7	7	7	2.06	507

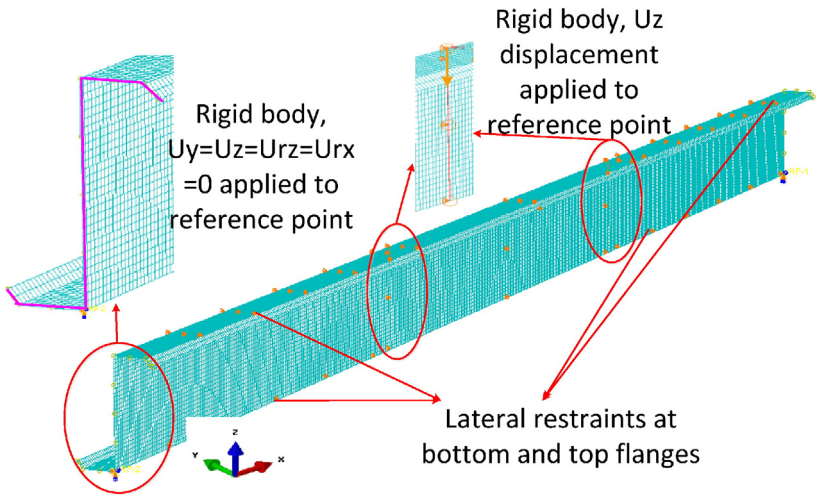

Fig. 12. FE model and boundary conditions.

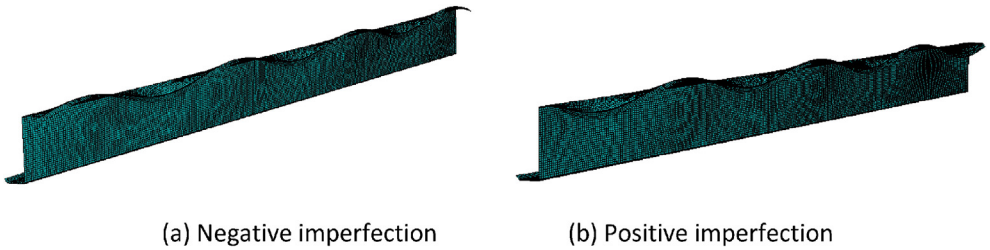

Fig. 13. Distortional imperfections in the FE model.

in Eq. (5). The design moment resistance of a laterally unrestrained beam is calculated as:

$$f(x) = \chi_{LT} \cdot W_{eff} \cdot f_y / \gamma_{M_0} \tag{13}$$

with

$$\chi_{LT} = \frac{1}{\Phi_{LT} + \sqrt{\Phi_{LT}^2 - \lambda_{LT}^2}} \leq 1.0 \tag{14}$$

and

$$\Phi_{LT} = 0.5\left[1 + 0.34\left(\overline{\lambda}_{LT} - 0.2\right) + \lambda_{LT}^2\right] \tag{15}$$

The optimisation was carried out for the first prototype (lipped channel), while considering four different lengths: 1, 2, 3 and 4 m. The optimised cross-sections and their corresponding flexural strengths are summarised in Figs. 6 and 7, respectively.

A comparison between the optimised results in Fig. 6 indicates that the flange width becomes larger with increasing unbraced length, and consequently, the total height of the section is diminished to keep the total coil width constant. This is due to the fact that longer beams are more susceptible to lateral-torsional buckling, and thus the dimensions of the flanges increase while the lips turn outwards to enhance the torsional stiffness and the minor axis bending stiffness. In contrast, beams with shorter spans are predominantly affected by the interaction of local/distortional buckling and lateral-torsional buckling, rather than failing purely in the global mode. It is noted that serviceability criteria (deflections) were not considered in this study and that the optimisation is solely carried out with respect to the ultimate capacity.

Fig. 7 compares the flexural capacity of the optimised and the initial lipped channel sections for all four lengths. It is shown that a considerable increase in flexural capacity can be achieved by using the proposed optimisation method. While, for the same amount of material, the flexural capacity of a 1 m long optimised beam is 26% higher than that of the standard section, the improvement is 75% for the 4 m long beam. Once again, none of the practical constraints in the rightmost column of Table 1 turned out to be critical.

It is worth mentioning that the optimisation was carried out assuming a uniform bending moment in the beam and assuming the previously defined boundary conditions. When the laterally unbraced beams are exposed to a different applied loading (reflected in a different elastic lateral-torsional buckling moment) or different boundary conditions, the optimal sections will change. Besides, for longer beam elements, serviceability limits (in particular: maximum deflections) may govern the design. While serviceability criteria were not considered in the current scope, the proposed optimisation framework using PSO algorithm can easily be adapted to incorporate serviceability limits.

Table 6
Comparison of the bending resistances obtained from FE analysis and experiment with different imperfection values in negative direction.

Specimen	Flexural strength (kN·m)				FE to experimental flexural strength		
	M_{test}	$M_{25\%}$	$M_{50\%}$	$M_{75\%}$	$M_{25\%}/M_{test}$	$M_{50\%}/M_{test}$	$M_{75\%}/M_{test}$
D8.5Z120-4	28.7	27.92	28.32	27.88	0.97	0.99	0.97
D8.5Z115-1	26.8	28.47	27.8	26.66	1.06	1.04	0.99
D8.5Z092-3	17.3	18.45	18.22	17.45	1.07	1.05	1.01
D8.5Z082-4	14.3	15.98	15.31	15.12	1.12	1.07	1.06
D8.5Z065-7	10.5	11.64	11.37	11.18	1.11	1.08	1.06
D8.5Z065-4	9	10.93	10.56	10.21	1.21	1.17	1.13
D11.5Z092-3	29.6	30.84	30.56	29.6	1.05	1.04	1.00
D11.5Z082-4	26.4	27.4	26.32	25.48	1.04	1.00	0.97
Average					1.08	1.06	1.02
St. dev.					0.07	0.06	0.06

Table 7
Comparison of the bending resistances obtained from FE analysis and experiment with different imperfection values in positive direction.

Specimen	Flexural strength (kN·m)				FE to experimental flexural strength		
	M_{test}	$M_{25\%}$	$M_{50\%}$	$M_{75\%}$	$M_{25\%}/M_{test}$	$M_{50\%}/M_{test}$	$M_{75\%}/M_{test}$
D8.5Z120-4	28.7	28.66	28.12	27.49	1.00	0.98	0.96
D8.5Z115-1	26.8	29.46	28.52	28.03	1.10	1.06	1.05
D8.5Z092-3	17.3	18.1	17.46	16.93	1.05	1.01	0.98
D8.5Z082-4	14.3	16.81	15.92	14.36	1.18	1.11	1.00
D8.5Z065-7	10.5	12.21	11.36	10.94	1.16	1.08	1.04
D8.5Z065-4	9	10.85	10.12	9.56	1.21	1.12	1.06
D11.5Z092-3	29.6	32.98	30.83	30.69	1.11	1.04	1.03
D11.5Z082-4	26.4	27.56	27.13	26.96	1.04	1.03	1.02
Average					1.11	1.06	1.02
St. dev.					0.07	0.05	0.04

6. Direct strength method (DSM)

The Direct Strength Method (DSM) is an alternative to the traditional effective width method to predict the load carrying capacity of CFS members. This method integrates a computational stability analysis into the design process. In a first step, the elastic local, distortional and global buckling loads are determined. Using these elastic buckling loads and the load that causes first yield, the strength is then directly predicted based on a series of simple empirical equations. While calculation of the effective properties can be tedious for complex CFS cross-sections, only

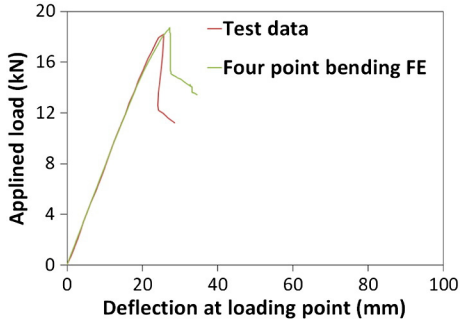

Fig. 14. Comparison between experimental results and FE analyses for laterally braced specimen D11.5Z092-3.

Table 8
Comparison of ultimate capacities obtained from FE analysis and experiment for laterally unbraced braced beams (lipped channels).

Specimen	h (mm)	b (mm)	t (mm)	r (mm)	d (mm)	Length (m)	Q (kN)	Q_{test} (kN)	Q_{test}/Q –
19L17e0	102	51	1.9	5	14.5	1.7	13.24	15.38	1.16
19L19e0	102	51	1.9	5	14.5	1.9	12.11	12.68	1.05
19L23e0	102	51	1.9	5	14.5	2.3	9.54	9.94	1.04
19L25e0	102	51	1.9	5	14.5	2.5	7.79	8.65	1.11
10L17e0	102	51	1	5	12.5	1.7	3.72	3.51	0.94
10L19e0	102	51	1	5	12.5	1.9	3.18	3.46	1.09
10L23e0	102	51	1	5	12.5	2.3	2.78	2.43	0.87
10L25e0	102	51	1	5	12.5	2.5	2.3	2.8	1.22
Average									1.06
St. dev.									0.11

gross section properties are needed in the DSM. The elastic buckling loads of CFS members can be calculated using software such as CUFSM [21]. A comprehensive review of the DSM, including a comparison with the effective width method, has been presented by Schafer [22].

In this study the flexural strengths of the optimised as well as the original sections were determined based on the DSM, for both laterally braced and laterally unbraced conditions, for the purpose of comparison with the Eurocode. The results are shown in Figs. 8 and 9. For the laterally braced beams, the flexural strength was determined as the minimum of the local and distortional strengths (Table 3). However, for laterally unbraced beams, the ultimate strength was determined based on the minimum of the local, distortional and lateral-torsional strengths (Table 4). The strength in local buckling thereby accounts for the possibility of local–global mode interaction.

For both laterally braced and unbraced conditions, the results obtained from the DSM confirm that the flexural strengths of the optimised shapes have been considerably improved compared to the original cross-sections. Comparison between the results predicted by the DSM and EC3 indicates that both methods show a very similar trend across the range of prototypes.

However, it should be mentioned that only prototypes ① (lipped channel) and ② (lipped channel with one intermediate stiffener in the web) are 'pre-qualified' cross-sections according to Appendix 1 of AISI [13]. This means that, in principle, the DSM should not be applied to prototypes ③-⑥.

7. Nonlinear FE analysis considering initial geometric imperfections

The flexural capacity of the optimised cross-sections in this study was also determined using detailed nonlinear FE analyses performed with ABAQUS [23]. The results were used to assess the adequacy and performance of the proposed optimisation procedure. In this section, a detailed description of the modelling approach is first presented, followed by its verification against experimental data available in the literature.

7.1. FE modelling

The FE models of the CFS sections were developed using a 4-node quadrilateral shell element with reduced integration (S4R). By performing sensitivity analyses, a mesh size of 10 mm was found to be optimal, so that further refinement did not result in any noticeable improvement in accuracy. However, smaller elements were used to model the rounded corner zones. The stress–strain behaviour of the CFS plates was simulated using the constitutive model proposed by Haidarali and Nethercot [24], which is illustrated in Fig. 10. This model is composed of the basic Ramberg–Osgood stress–strain relationship up to the 0.2% proof stress, followed by a straight line with a constant slope of $E/50$, where E stands for the elastic modulus. In this model, the relationship between stress, σ, and strain, ε, is mathematically expressed as:

$$\begin{aligned} \varepsilon &= \frac{\sigma}{E} + 0.002\left(\frac{\sigma}{\sigma_{0.2}}\right)^n \qquad \text{for } \sigma \le \sigma_{0.2} \\ \varepsilon &= \varepsilon_{0.2} + \frac{50(\sigma-\sigma_{0.2})}{E} \qquad \text{for } \sigma \ge \sigma_{0.2} \end{aligned} \tag{16}$$

where $\sigma_{0.2}$ is the 0.2% proof stress, $\varepsilon_{0.2}$ is the total strain at a stress $\sigma_{0.2}$, n is a shape parameter recommended by Gardner and Ashraf [18] to be taken as 28 for grades 350 and 450 steel, and E is the elastic modulus which is taken equal to 210 GPa.

The solution was obtained using the displacement control method which has previously been shown capable of adequately modelling large deformations in the post-buckling range [23].

7.2. Experimental verification of the FE model

7.2.1. Laterally braced beams

For the purpose of verifying the FE modelling approach with respect to CFS members failing by local/distortional buckling, the four-point bending distortional buckling tests performed by Yu and Schafer [25, 26] were selected. Fig. 11 presents a schematic illustration of the test

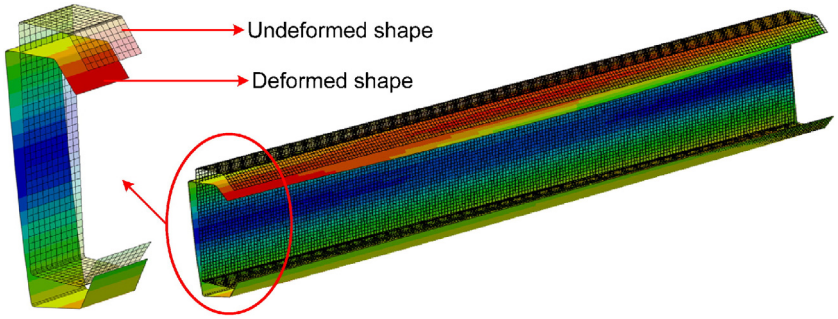

Fig. 15. CFS beam with negative lateral-torsional imperfection.

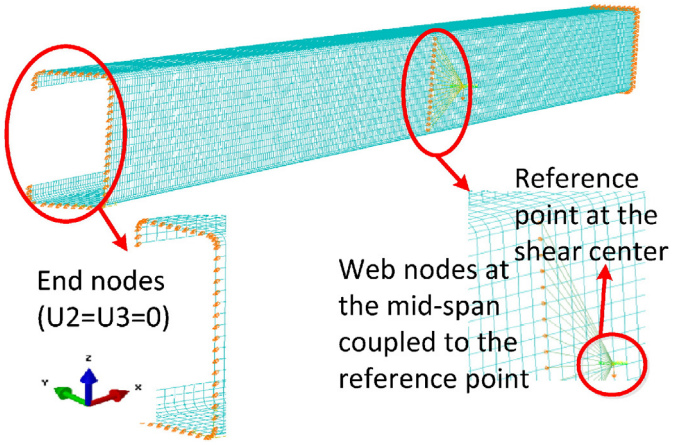

Fig. 16. FE model and boundary conditions for laterally unbraced beams.

set-up and also shows the cross-section of the test specimens. This test set-up was designed to prevent global buckling and, therefore, the test specimens acted as laterally braced beams.

The total length of the test specimens was 4878 mm, and the top and bottom flanges of the beams were unrestrained in the middle 1626 mm long span to allow distortional buckling to occur. The dimensions of the cross-section and their material properties are summarised in Table 5.

The beams were modelled using hinged boundary conditions about the horizontal axis, while the rotations about the vertical axis were prevented, as shown in Fig. 12. The end sections were also fixed against warping (Fig. 12) to prevent lateral-torsional buckling in the FE model. At both ends of the beam, the displacements of the end section nodes were coupled to those of the bottom corner using a single point constraint (SPC). The cross-sections underneath the application points of the load were defined as rigid bodies in order to prevent localised failure. Vertical downward displacements were then imposed on the reference points of these rigidised cross-sections at the top corners of the web. These boundary conditions are similar to the ones previously adopted by Haidarali and Nethercot [24].

Residual stresses were not included in the model. It has previously been demonstrated that the effects of membrane residual stresses can safely be neglected in open sections [27,28], while the (longitudinal) bending residual stresses are implicitly accounted for in the coupon test results, provided that the coupons are cut from the fabricated cross-section rather than from the virgin plate. Indeed, cutting a coupon releases the bending residual stresses, causing the coupon to curl [29]. However, these stresses are re-introduced when the coupon is straightened under tensile loading in the initial stages of the coupon test. Apart from introducing residual stresses, the cold-rolling process has the effect of increasing the material yield stress through work-hardening. This effect is most pronounced in the corner regions of the cross-sections. Schafer and Moen [27] have in this respect proposed that, when residual stresses are not modelled, the increased properties of the corner regions should also not be modelled. Their rationale is that, while both effects have a relatively minor influence on the ultimate capacity, the detrimental effect of the residual stresses will largely be offset by the gain in capacity resulting from the work-hardened corners. Their recommendation was followed in this paper.

The FE analysis included the effects of geometric imperfections. The local, distortional and global buckling modes were generated using the CUFSM finite strip software [21]. The same cross-sectional discretization as in the FE mesh was employed in CUFSM. Sinusoidal functions with a wavelength equal to the critical local/distortional wavelength obtained from CUFSM were then used to propagate the cross-sectional local/distortional imperfection along the beams by adjusting the nodal coordinates of the FE mesh. It was thereby necessary to slightly adjust the wavelength in order to obtain an integer number of half-waves.

The local and distortional imperfections were multiplied with a scale factor and superimposed. The magnitudes of the local and distortional imperfections were based on the cumulative distribution function (CDF) values proposed by Schafer and Peköz [27]. Three different CFD values (i.e. 25%, 50%, and 75%) were considered, in both a positive and a negative direction, according to the convention shown in Fig. 13, in order to study their effect on the load carrying capacity.

A comparison of the experimental moment capacities with those obtained from FE analysis for the three different CDF values is provided in Tables 6 and 7, for negative and positive imperfections, respectively. It is seen that, in general, good agreement was obtained between the models and the experimental results. The error was, on average, less than 7% for both positive and negative imperfections. The magnitude of the imperfection, in this particular case, did not seem to have a major impact on the load-carrying capacity. In the remainder of this study, CDF values of 50% were used. This magnitude represents the 'most probable' imperfection and has also been suggested by other researchers (e.g. [24]).

The experimental load–deflection response of specimen D11.5Z092-3 (Table 7) is compared to the FE predictions in Fig. 14. The results confirm the accuracy of the FE model in predicting the bucking and post-buckling behaviour of the CFS member, including its stiffness, ultimate strength and deflection at the peak load.

7.2.2. Laterally unbraced beams

The FE models of the laterally unbraced beams were verified against tests conducted by Put et al. [30]. Table 8 shows the dimensions of the eight test specimens. In the experiment a special frame was attached to the cross-section at mid-span in order to apply the load through the shear centre by means of incremental weights. The beams were simply supported at their ends. The local/distortional imperfections of the test specimens were not measured and, in an identical approach to the one reported in Section 7.2.1, local and distortional imperfections with a CDF value of 50% were used in the FE model. An overall imperfection in the shape of the lateral-torsional mode with an amplitude of L/1000 was also added [31]. It was thereby found that, generally, adding a negative imperfection (with the cross-section rotated as shown in Fig. 15) resulted in a lower ultimate moment capacity in the unbraced

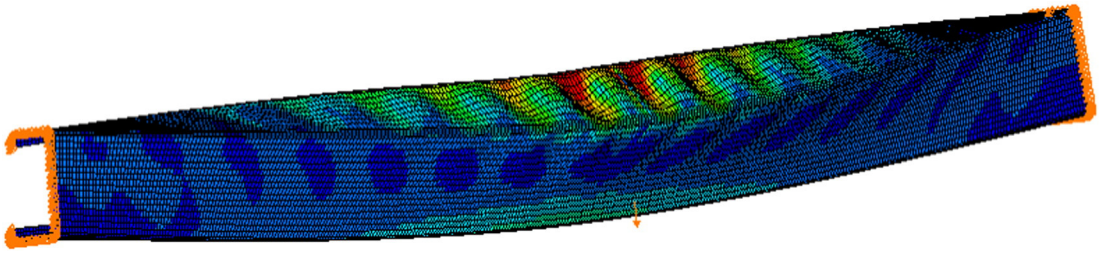

Fig. 17. Typical failure mode of laterally unbraced beams (specimen 10L17e0 at ultimate load).

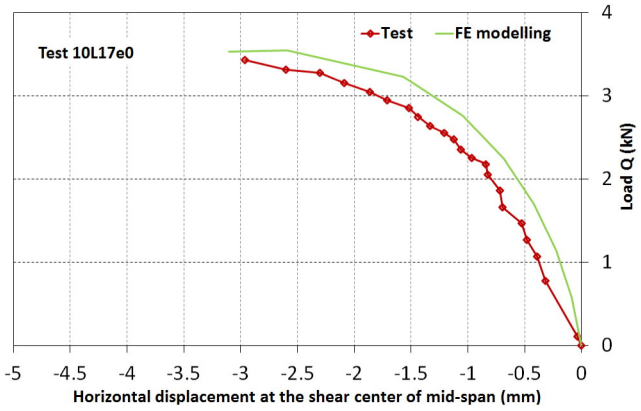

Fig. 18. Comparison between experimental results and FE analysis for laterally unbraced specimen 10L17e0.

channels and was therefore more critical. Similar observations were reported by Kankanamge and Mahendran [31]. Therefore, only negative imperfections were considered in the FE studies covered in this paper. Fig. 16 illustrates the FE model and the boundary conditions. A reference point was defined at the shear centre of the cross-section at mid-span and all the nodes of the web at the mid-span section were coupled to the reference point using rigid beams. A downward displacement was then imposed on the reference node without restricting its lateral displacement.

The typical failure mode of the unbraced beams in the FE model was interaction of local buckling and lateral-torsional buckling, as illustrated in Fig. 17. This is consistent with the experimental results reported by Put et al. [30]. Table 8 compares the ultimate capacities of the laterally unbraced braced beams obtained from the FE analyses to the experimental values. It shows that, on average, the FE models predict the ultimate strength of the laterally unbraced beams with less than 6% error. The load vs. lateral displacement curves from both the experiment and the FE analysis are shown in Fig. 18 for specimen 10L17e0. The graph shows very good agreement between the FE model and the test results.

Table 9
The critical buckling modes and the buckling half-wave length for laterally restrained beams.

Section	Buckling half-wave length (mm)		Buckling moment (kN·m)	
	Local	Distortional	Local	Distortional
Standard	100	400	4.79	4.81
Opt①	120	600	4.12	6.09
Opt ②	80	600	16.99	7.18
Opt ③	100	500	7.14	6.08
Opt ④	100	500	4.31	5.69
Opt ⑤	100	600	7.43	8.57
Opt ⑥	120	600	8.80	8.60

7.3. FE simulations of the optimised channel sections

The experimentally validated FE models were subsequently used to evaluate the efficiency of the optimised channel sections obtained in Section 5 and make a comparison with their standard counterpart.

7.3.1. Laterally braced beams

In the FE model, the laterally restrained beams were observed to fail by local and/or distortional buckling. As suggested by Shifferaw and Schafer [32], the length of the FE models of both the optimised and the standard sections was taken as three times the distortional buckling half-wave length calculated using the CUFSM [21] software. This was generally short enough to avoid lateral-torsional buckling. With respect to the boundary conditions, the member was pin-ended about the major axis and prevented from rotating about the minor axis, while the end sections were prevented from warping. Equal but opposite rotations were applied at both ends. Fig. 19 illustrates the boundary conditions and loading of the FE models. Local/distortional imperfections with an amplitude corresponding to the 50% value of the CDF were used. Table 9 summarises the local and distortional critical moments and the associated buckle half-wave lengths of the standard and optimised cross-sections of different prototypes obtained from CUFSM. The flexural strength of the optimised and the standard cross-sections obtained from FE analyses are compared in Fig. 20.

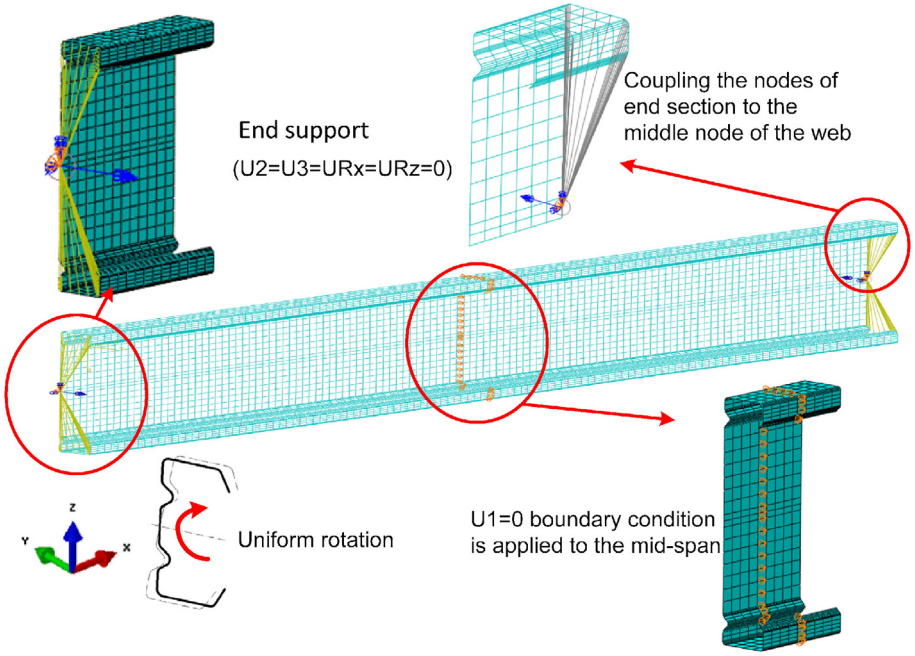

Fig. 19. Boundary conditions in the FE models of channel sections.

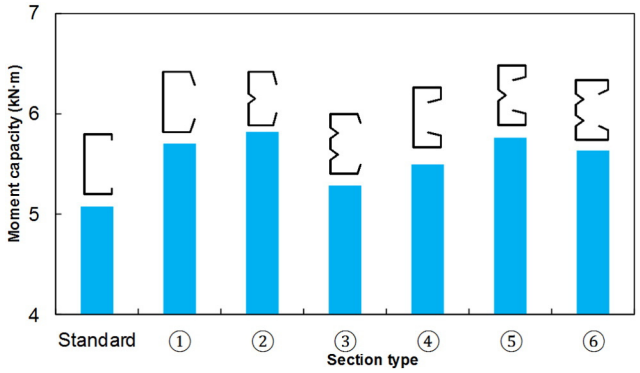

Fig. 20. Comparison of FE predicted strengths of optimised and standard cross-sections for laterally braced beams.

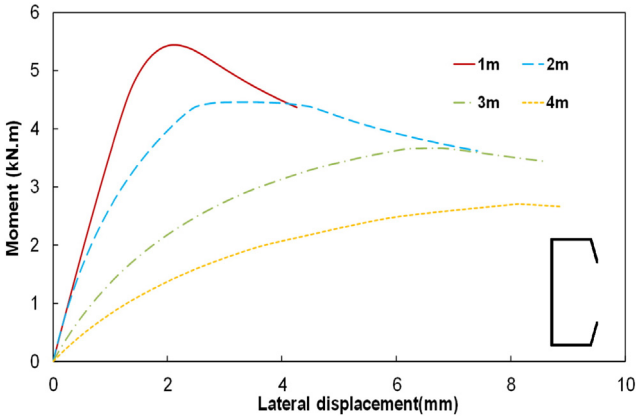

Fig. 22. Moment-lateral deflection curves at mid-span of the optimised unbraced beams.

The results confirm that a considerable increase in the flexural capacity can be observed in the optimised shapes compared to the standard sections possessing the same amount of material (i.e. the same total coil width and thickness).

7.3.2. Laterally unbraced beams

The laterally unbraced beams were assumed to be simply supported at the ends (with respect to both in-plane and out-of-plane rotations) with no lateral restraints in between. Warping of the end sections was free to occur and the load was applied by imposing an end rotation about the major axis, as shown in Fig. 21. Four different lengths (i.e. 1 m, 2 m, 3 m, and 4 m) were considered, both for the standard and the optimised CFS cross-sections. Local/distortional imperfections were modelled and combined with an overall imperfection of L/1000 in the shape of the lateral-torsional buckling mode [31].

The (uniform) bending moments obtained from the FE analysis are plotted in Fig. 22 against the lateral displacement (at mid-span) of the optimised beams with four different lengths. The moment-lateral displacement curves illustrate the obvious fact that increasing the length of the CFS beams results in a decrease of the bending capacity due to lateral torsional buckling.

The flexural strengths of the optimised and the standard cross-sections with different lengths obtained using FE analyses are compared in Fig. 23. Confirming the results obtained from the effective width method in EC3, Fig. 23 shows that the optimised shapes offer a much higher flexural capacity (up to 108% higher) compared to the standard sections with the same amount of material, particularly in longer beams where global buckling is the dominant mode.

8. Reliability of the EC3 based approach

The results obtained from the experimentally validated FE models were treated as a benchmark to evaluate the accuracy of the DSM and the effective width method implemented in EC3. The EC3 and DSM predicted flexural strengths of the standard lipped channel and the optimised cross-sections obtained for all six prototypes (see Table 1) are compared in Table 10 for the laterally braced elements. For comparison purposes, the strength values are normalised with respect to the flexural strength obtained from FE analysis.

The results obtained from EC3 and from the DSM are both in good agreement with their FE counterparts. However, for the laterally braced beams, the DSM provided slightly more accurate and slightly more conservative estimates of the strengths than EC3. EC3 overestimated the flexural capacity of the laterally braced sections by 11% on average.

For the unbraced beams, however, the findings are reversed. It is shown in Table 11 that the strengths calculated based on EC3 are conservative for the unbraced beams, while the DSM overestimated the flexural capacity of both the standard and the optimised sections by up to 36% and by 21% on average. Table 11 also indicates that the accuracy of the DSM decreased with increasing span length.

The FE simulations carried out in this study generally confirmed the accuracy of the EC3 design rules and therefore its suitability to be used as a tool for optimisation. It is thereby noted that using EC3 as a basis

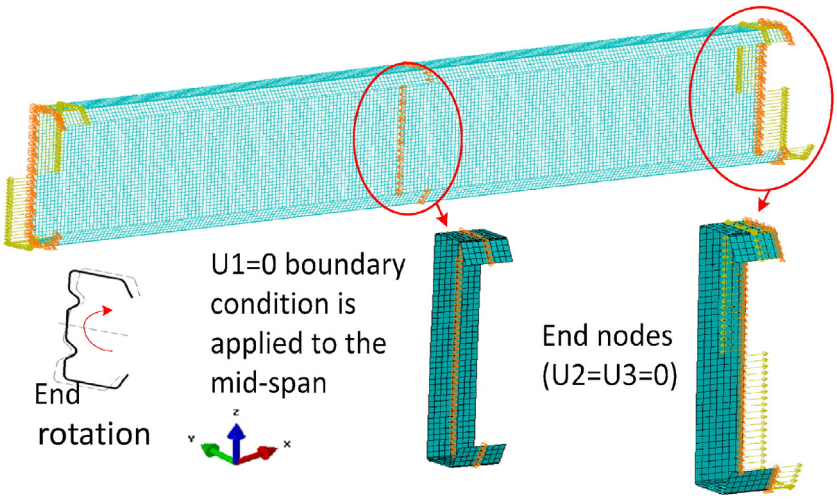

Fig. 21. FE model for laterally unbraced standard and optimise beams.

for optimisation leads to a significant simplification of the process compared to the effort it would take to use detailed non-linear FE analyses as part of the optimisation process.

As a final summary, Fig. 24(a) and (b) compare the ultimate capacities obtained using EC3, the DSM and the FE models, made dimensionless with respect to the capacity of the standard section obtained using the same method, for all braced and unbraced channel beams. It is shown that, while the EC3 predicts gains which are consistently about 10% higher than the FE/DSM predictions for the braced beams, a very good match is obtained for the unbraced beams. Most importantly, however, the trends of increasing/decreasing capacity over the range of prototypes (for the braced beams) and over the range of lengths (for the unbraced beams) are very well predicted by EC3 when the FE simulations are taken as a benchmark. In particular, the EC3 predicted conclusion that prototype 2 is the most efficient prototype for unbraced beams, is confirmed by the FE models. In general, the results indicate that the proposed optimisation method is accurate and reliable and provides a practical tool for manufacturers and structural engineers to optimise the capacity of CFS elements.

By optimizing each CFS beam in a given structure for a particular length and boundary conditions, a structure with minimum weight and optimal material efficiency could be obtained. However, in reality it would not be economical to custom roll each individual member, since a definite cost is incurred when reconfiguring the rolling process. Moreover, smaller roll-forming companies might not have this capability in the first place. Considering the range of optimum sections over lengths from 1 m to 4 m (Fig. 6), a question of a very practical nature could be which section to commercialize and mass-produce as a 'general purpose section'. In the authors' design experience, the effective lengths of roof purlins, after taking into account the rotational restraint of the cladding (and given the reality in the UK that the market for roof cladding is almost monopolized by a single type of roofing panel), usually range from 1.5 m to 2.5 m. Therefore, the optimum section proposed for a 2 m length would be a good candidate for a commercial roof purlin.

9. Summary and conclusions

This paper presents a practical method to obtain more economical CFS channel sections for use as laterally braced or unbraced beams by optimising the dimensions of the cross-section and allowing for the addition of double-fold (return) lips, inclined lips and triangular web stiffeners. The optimisation process is thereby based on the Particle Swarm Optimisation (PSO) Algorithm, while the flexural strength of the sections is determined using the effective width method as implemented in EC3. Six different prototypes were considered based on practical considerations. Based on the results of this study, the following conclusions could be drawn:

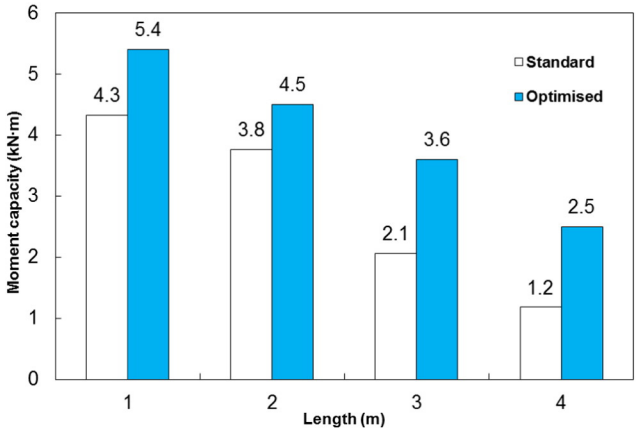

Fig. 23. Comparison of FE predicted flexural strengths of optimised and standard cross-sections for laterally unbraced beams.

Table 10
Comparison of predicted strengths with FE results for laterally braced beams.

Strength ratio	Section							Average	St. dev.
	Standard	①	②	③	④	⑤	⑥		
EC3/FEM	1.07	1.09	1.16	1.15	1.12	1.14	1.08	1.11	0.036
DSM/FEM	0.98	0.92	0.98	0.98	0.96	1	0.99	0.97	0.028

(1) By applying the proposed optimisation method to laterally braced beams, significant gains in cross-sectional bending capacity can be achieved: in the example, the bending capacity of a CFS cross-section was increased by up to 25% compared to the commercially available section taken as a starting point. The most effective cross-sectional prototype in this case was the lipped channel section with one stiffener located in the web. Using two stiffeners in a symmetrical arrangement, while keeping the developed length constant, would again reduce the efficiency of the solution.

(2) The flexural capacity of the optimised 1 m, 2 m, 3 m and 4 m long unbraced beams was increased by 26%, 25.8%, 61% and 75%, respectively, compared to a commercially available section with the same amount of material. Comparison between the optimised results indicated that, when increasing the unbraced length, the flange width of the optimum solution increased, and consequently the total height of the section was reduced.

(3) The adequacy of the optimised sections was verified using detailed nonlinear FE analyses validated against experimental data, while also taking into account the effects of initial imperfections. The FE results, on average, showed less than a 6% error compared with the experimental data. The FE results of the commercially available and the optimised sections for both laterally braced and unbraced conditions generally showed good agreement with the flexural strengths estimated by EC3. The FE simulations also closely followed the increasing or decreasing trends in flexural capacity predicted by EC3 across the different prototypes. This demonstrates the reliability of the proposed optimisation method using the EC3 design rules.

(4) The flexural strengths of the optimised and the commercially available sections were also determined based on the DSM. Overall, the strengths calculated using EC3 and the DSM displayed a similar trend. Compared to the FE results, EC3 overestimated the flexural strength of the laterally braced beams by up to 16%, but underestimated the strength of the laterally unbraced beams by up to 19%. While the DSM, in general, provided accurate estimates of the capacities of the laterally braced beams, the accuracy of the method was seen to decrease with an increase of unbraced span length. It was shown that the DSM may overestimate the flexural capacity of long span laterally unbraced beams by up to 36%.

Acknowledgement

This work was supported by the Engineering and Physical Sciences Research Council (EPSRC) grant EP/L019116/1. The authors would like to thank the EPSRC for their financial support.

Table 11
Comparison of predicted strengths with FE results for laterally unbraced beams.

Length (m)	Standard section		Optimised section	
	EC3/FEM	DSM/FEM	EC3/FEM	DSM/FEM
1	0.97	1.15	0.98	1.02
2	0.82	1.05	0.87	1.16
3	0.87	1.24	0.81	1.28
4	1.02	1.25	0.84	1.36
Average	0.92	1.17	0.88	1.21
St. dev.	0.091	0.093	0.074	0.148

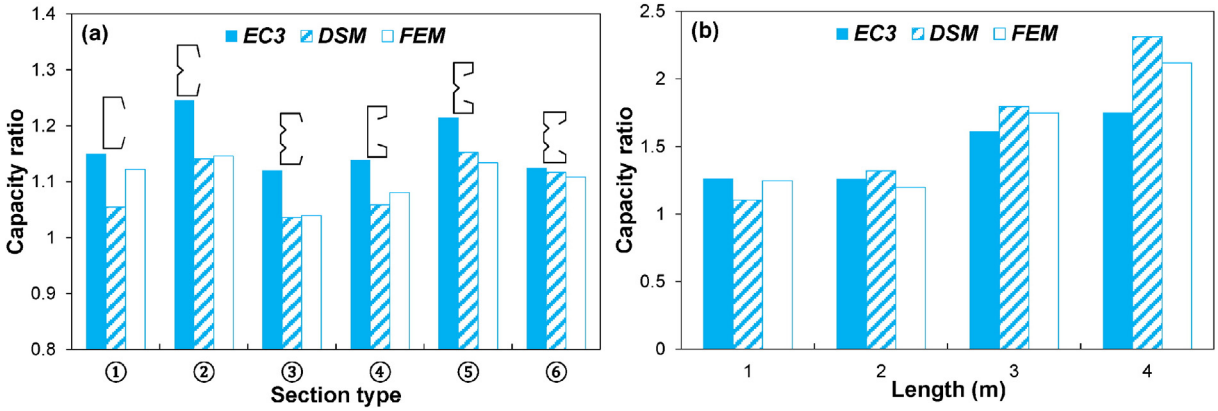

Fig. 24. Flexural strength ratio of the optimised sections to the standard section for (a) laterally braced beams and (b) for laterally unbraced beams using the same amount of material.

References

[1] H. Liu, T. Igusa, B.W. Schafer, Knowledge-based global optimization of cold-formed steel columns, Thin-Walled Struct. 42 (2004) 785–801.
[2] M. Moharrami, A. Louhghalam, M. Tootkaboni, Optimal folding of cold formed steel cross sections under compression, Thin-Walled Struct. 76 (2014) 145–156.
[3] J.Z. Leng, Z.J. Li, J.K. Guest, B.W. Schafer, Shape optimization of cold-formed steel columns with fabrication and geometric end-use constraints, Thin-Walled Struct. 85 (2014) 271–290.
[4] H. Adeli, A. Karim, Neural network model for optimization of cold-formed steel beams, J. Struct. Eng. ASCE 123 (1997) 1535–1543.
[5] J. Lee, S.-M. Kim, H.-S. Park, B.-H. Woo, Optimum design of cold-formed steel channel beams using micro-genetic algorithm, Eng. Struct. 27 (2005) 17–24.
[6] J. Lee, S.-M. Kim, H. Seon Park, Optimum design of cold-formed steel columns by using micro genetic algorithms, Thin-Walled Struct. 44 (2006) 952–960.
[7] T. Tran, L.Y. Li, Global optimization of cold-formed steel channel sections, Thin-Walled Struct. 44 (2006) 399–406.
[8] K. Magnucki, P. Paczos, Theoretical shape optimization of cold-formed thin-walled channel beams with drop flanges in pure bending, J. Constr. Steel Res. 65 (2009) 1731–1737.
[9] W. Ma, J. Becque, I. Hajirasouliha, J. Ye, Cross-sectional optimization of cold-formed steel channels to Eurocode 3, Eng. Struct. 101 (2015) 641–651.
[10] CEN, Eurocode 3: Design of Steel Structures, Part 1.3: General Rules—Supplementary Rules for Cold Formed Members and Sheeting, European Comittee for Standardization, Brussels, 2005.
[11] CEN, Eurocode 3: Design of Steel Structures, Part 1–5: Plated Structural Elements, European Comittee for Standardization, Brussels, 2005.
[12] CEN, Eurocode 3: Design of Steel Structures. Part 1–1: General Rules and Rules for Buildings, European Comittee for Standardization, Brussels, 2005.
[13] AISI, North American Specification for the Design of Cold-formed Steel Structural Members, 2007 ed. AISI S100-07, Washington, DC, 2007.
[14] AS/NZS, Cold-formed Steel Structures, AS/NZS 4600, Joint Technical Committee BD-082, Sydney, 1996.
[15] R. Hassan, B. Cohanim, O. De Weck, G. Venter, A comparison of particle swarm optimization and the genetic algorithm, Proceedings of the 1st AIAA Multidisciplinary Design Optimization Specialist Conference 2005, pp. 18–21.
[16] S. Jeong, S. Hasegawa, K. Shimoyama, S. Obayashi, Development and investigation of efficient GA/PSO-hybrid algorithm applicable to real-world design optimization, IEEE Comput. Intell. Mag. 4 (2009) 36–44.
[17] R.E. Perez, K. Behdinan, Particle swarm approach for structural design optimization, Comput. Struct. 85 (2007) 1579–1588.
[18] L. Gardner, M. Ashraf, Structural design for non-linear metallic materials, Eng. Struct. 28 (2006) 926–934.
[19] Mathworks, Matlab R2011a, Mathworks, Inc., 2011
[20] J. Ye, I. Hajirasouliha, J. Becque, K. Pilakoutas, Development of more efficient cold-formed steel channel sections in bending, Thin-Walled Struct. 101 (2016) 1–13.
[21] B. Schafer, CUFSM Version 3.12, Department of Civil Engineering, Johns Hopkins University, 2006 (http://www.ce.jhu.edu/bschafer/cufsm/).
[22] B.W. Schafer, Review: the direct strength method of cold-formed steel member design, J. Constr. Steel Res. 64 (2008) 766–778.
[23] ABAQUS, in, Hibbitt, Karlsson & Sorensen, Inc., Pawtucket, USA, 2007.
[24] M.R. Haidarali, D.A. Nethercot, Finite element modelling of cold-formed steel beams under local buckling or combined local/distortional buckling, Thin-Walled Struct. 49 (2011) 1554–1562.
[25] C. Yu, B.W. Schafer, Simulation of cold-formed steel beams in local and distortional buckling with applications to the direct strength method, J. Constr. Steel Res. 63 (2007) 581–590.
[26] C. Yu, B.W. Schafer, Distortional buckling tests on cold-formed steel beams, J. Struct. Eng. ASCE 132 (2006) 515–528.
[27] B.W. Schafer, T. Pekoz, Computational modeling of cold-formed steel: characterizing geometric imperfections and residual stresses, J. Constr. Steel Res. 47 (1998) 193–210.
[28] B.W. Schafer, Z. Li, C.D. Moen, Computational modeling of cold-formed steel, Thin-Walled Struct. 48 (2010) 752–762.
[29] M. Jandera, L. Gardner, J. Machacek, Residual stresses in cold-rolled stainless steel hollow sections, J. Constr. Steel Res. 64 (2008) 1255–1263.
[30] B.M. Put, Y.L. Pi, N.S. Trahair, Lateral buckling tests on cold-formed channel beams, J. Struct. Eng. ASCE 125 (1999) 532–539.
[31] N.D. Kankanamge, M. Mahendran, Behaviour and design of cold-formed steel beams subject to lateral-torsional buckling, Thin-Walled Struct. 51 (2012) 25–38.
[32] Y. Shifferaw, B.W. Schafer, Inelastic bending capacity of cold-formed steel members, J. Struct. Eng. ASCE 138 (2012) 468–480.